BL11XU
(QST Quantum Dynamics I)

1. Abstract

BL11XU is an in-vacuum undulator beamline operated by National Institutes for Quantum and Radiological Science and Technology (QST). In this beamline, a switchable Si(111) and Si(311) double-crystal monochromator cooled by liquid nitrogen is installed in the optical hutch. Highly brilliant and directional synchrotron X-rays are available in the energy range of 6–70 keV. The experimental hutch contains four kinds of specialized measurement instruments for studies using Mössbauer spectroscopy (EH 1), inelastic X-ray scattering (EH 2), X-ray magnetic circularly polarized emission (EH 2), and surface X-ray diffraction (EH 3). This beamline provides scientists and engineers with a wide range of options on advanced synchrotron radiation research and quantum functional material research.

2. Mössbauer spectroscopy

Mössbauer spectroscopy is used as a powerful method in various fields such as physics, chemistry, biology, and earth science [1]. The Mössbauer effect, which is the principle behind this method, was first discovered using the nuclear resonance of ^{191}Ir. Since then 86 nuclides of 45 elements have exhibited a Mössbauer effect [2]. Since the 1970's, synchrotron radiation (SR) has been used as a source for Mössbauer spectroscopy [3, 4]. The white energy property of SR, which typically extends to 100 keV, is suitable for Mössbauer spectroscopy of those nuclides. In addition, its high brilliance, low angular divergence, and high polarization are applicable to Mössbauer studies on various samples under diverse situations such as high pressure and an *in situ* gas atmosphere. To improve the applicability of SR Mössbauer spectroscopy, we recently conducted a feasibility study on the SR-based Mössbauer absorption spectroscopy of ^{99}Ru, which is a high-energy nuclide.

^{99}Ru conventional Mössbauer spectroscopy has been usually performed using a radioisotope (RI) source since the first experiment by Kistner [5]. However, the nuclides have some undesirable properties. For example, the natural abundance of ^{99}Ru is only 12.7% and the recoilless fraction of samples is often low due to the high resonance energy of the first excited state of ^{99}Ru (89.57 keV) [6]. One superior property is its narrow energy width, which corresponds to the half-life of the excited state (20.5 ns). The width is sufficiently narrow to evaluate the valence via the isomer shift. The RI source in the conventional method is ^{99}Rh, which is synthesized by ^{99}Ru (p, n) ^{99}Rh reaction, whose half-life is about 16 days. In this study, we challenge the first observation of the SR-based Mössbauer absorption spectrum of ^{99}Ru nuclei.

The experiments were performed at BL11XU in SPring-8. Figure 1 shows the experimental setup. The electron bunch mode of the storage ring was also the 203 bunch mode. The SR from the undulator was monochromatized by the Si(333) high heat load monochromator (HHLM). Then the SR penetrated the Cu attenuator and was diffracted by another Si(111) monochromator to eliminate the low energy SR.

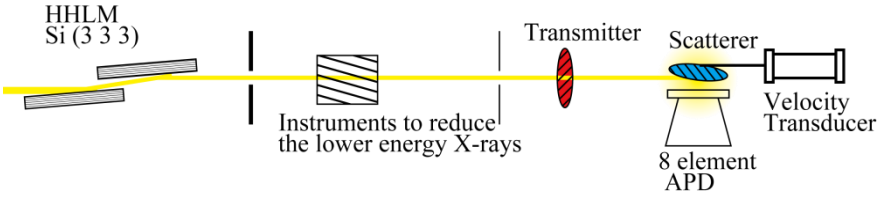

Fig. 1. Schematic of the measurement system for SR-based ^{99}Ru Mössbauer absorption spectroscopy. Instruments to reduce the lower-energy X-rays are the Cu attenuator and Si(111) monochromator. Transmitter is fcc-Ru NPs, and the scatterer is bulk hcp-Ru.

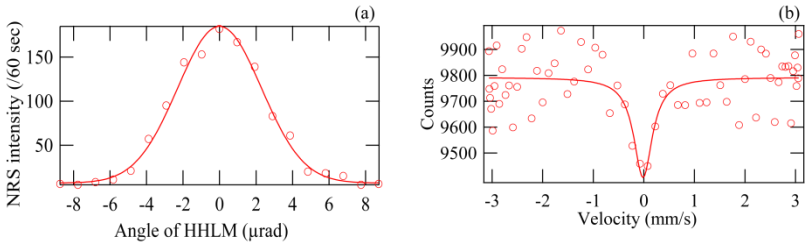

Fig. 2. Results of SR-based Mössbauer absorption spectroscopy using ^{99}Ru. (a) Intensity dependence on the Bragg angle. (b) Mössbauer spectrum of fcc-Ru NP vs. bulk hcp-Ru. Open circles are experimental data and the lines are fitting curves in both figures.

The SR penetrated the transmitter sample, forming natural Ru nanoparticles (NPs) with a face-centered cubic (fcc) structure, which differed from the bulk hexagonal closed packed (hcp) Ru structure. The average sizes of the NPs were 2.6 ± 0.5 nm. These NPs were synthesized by the chemical reduction method. This sample was not enriched, and NPs, including 100.4 mg Ru component, were shaped into a 5-mm-diameter pellet. It was arranged into a helium cryostat and its temperature was 4 K. SR was incident on the scatterer, which was bulk hcp-Ru metal. A pellet, which was 7-mm-diameter and contained 19.7 mg of the 95.5% enriched ^{99}Ru bulk powder, was 8° inclined to the beam direction. It was arranged into a vacuum chamber and cooled to around 45 K by a refrigerator. It was also connected with a Mössbauer velocity transducer to control the energy of its nuclear resonance. The scattering from the scatterer, including internal conversion electrons, was detected by an array of eight APD detectors.

The intensity of the nuclear resonance detected by the APD detector was 3 cps (Fig. 2a). With this counting rate, the SR-based Mössbauer absorption spectra of fcc-Ru NPs vs. bulk hcp-Ru was measured (Fig. 2b). Although it takes 72 h to measure the spectrum, the statistical errors in the spectrum are not small. However, the hyperfine structure could be evaluated with the following reasonable assumption: fcc-Ni NPs did not show quadrupole splitting or a magnetic hyperfine structure because bulk hcp-Ru showed none of these hyperfine structures. The isomer shift was estimated to be −0.04 ± 0.06 mm/s under this assumption and the valence state of fcc-Ru NP was not different from that of bulk hcp-Ru within the experimental error. Considering the typical isomer

shift value shown in Ref. 7, where the typical isomer shift difference corresponded to one electric valence (for example, between Ru^{3+} and Ru^{4+}), was more than 0.1 mm/s, the valence states of the Ru atom could be discussed using this spectrum. Here, the FWHM of 0.5 ± 0.3 mm/s is reasonable when we consider the effective thickness of the samples using the recoilless fraction of Ru metal based on Ref. 8. Recently, Ru thin films with thicknesses of 2.5–12 nm forming body-centered tetragonal (bct) structures showed ferromagnetism even at room temperature [9]. However, such magnetization was not detected in fcc-Ru NPs despite their smaller size.

In this study, the SR-based Mössbauer absorption spectrum with ^{99}Ru was observed for the first time. It demonstrates that the SR-based Mössbauer absorption spectra can be obtained with nuclides whose nuclear resonant energy is around 90 keV, even if the transmitter samples are composed of non-enriched elements. The fcc-Ru NPs show the same isomer shifts as that of bulk hcp-Ni within a reasonable experimental error.

In another experiment using this method, we successfully observed the synchrotron radiation Mössbauer absorption spectrum of the ^{158}Gd nucleus, whose resonant energy was 86.5 KeV. In the near future, improvements of the measurement system will realize ^{99}Ru and ^{158}Gd SR-based Mössbauer absorption spectroscopies of various complex materials.

3. Inelastic X-ray scattering

One of the main activities in EH 2 is to study element-selective and momentum-resolved electronic excitations in transition-metal compounds, especially in strongly correlated transition-metal oxides using resonant inelastic X-ray scattering (RIXS) at the K-edge of the 3d transition metal and the L-edge of the 5d transition metal [10, 11]. These absorption edges are located in the hard X-ray regime, and an inelastic scattering spectrometer for hard X-rays is installed in the hutch. Observations of the excitations enable one to clarify electronic interactions that govern the electronic properties. Another activity using the spectrometer is to investigate the electronic states of functional materials such as catalysts and electrodes in the battery by means of X-ray emission spectroscopy (XES) or high-energy-resolution fluorescence-detected X-ray absorption spectroscopy (HERFD-XAS) [12, 13]. Taking advantage of the high transmission of the hard X-rays one can measure spectra of the materials under *operando* conditions, leading to a guiding principle to improve the functions.

The analyzer is a key component to ensure the performance of a spectrometer. The energy of the scattered or emitted photons in a certain range of the solid angle is resolved in an angle-dispersive manner, namely, the energy is determined by the Bragg angle of the spherically-bent analyzer crystal. If a high energy resolution is required, the analyzer crystal is diced into small blocks to release the stress of the lattice. We are fabricating diced analyzers in-house following a procedure developed at the Advanced Photon Source [14].

The spectrometer at BL11XU can mount three analyzers. This year, we completed the fabrication of three analyzers for Ge(111) crystal. The Bragg angle of the Ge(333) reflection matches the energy of the Mn Kα emission, and the analyzers were used for *operando* HERFD-XAS of Mn_{12} molecular-cluster batteries.

4. X-ray magnetic circularly polarized emission

In response to the demand for observations of magnetic domains well below the surface of a specimen, we have been developing a magnetic microscope utilizing an X-ray magnetic circularly polarized emission (XMCPE) at BL11XU. XMCPE is a recently reported magnetooptical effect in the X-ray emission [15]. A large flipping ratio around 20% in the hard X-ray region is suitable for observations of magnetic domains located inside materials.

Crucial components of an XMCPE microscope are (i) the focusing optics, (ii) collimating optics, and (iii) circular polarization analyzer (Fig. 3). The lateral resolution is reduced by the focusing optics, and two compound refractive lenses were equipped. The focus size of each lens, which was measured by a wire scan, is about 10 μm. The collimating optics transforms a divergent fluorescence X-ray beam into a well-collimated X-ray beam. We employed a laterally graded multilayer Montel mirror. The acceptance angle of the mirror is 21 mrad × 21 mrad, and the multilayer period is tuned for 6.4 keV (Fe *K*α emission). The circular polarization analyzer consists of a phase plate (diamond 220) and a linear polarization analyzer (Ge 440). The diamond phase plate converts the circular polarization to linear polarization, and the converted linear polarization is evaluated by the linear polarization analyzer. The obtained linear polarization agrees with the initial circular polarization.

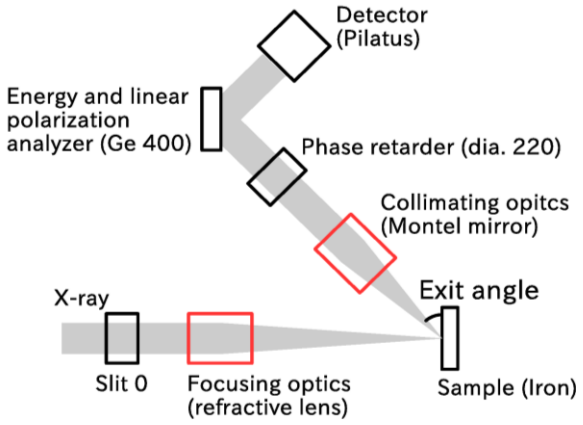

Fig. 3. Schematic of the XMCPE microscope in BL11XU.

We performed magnetic domain observations of a grain-oriented electrical steel sheet using this microscope. The step size was 30 μm (*x*) and 65 μm (*z*). About 5000 points were measured. The measurement time per point was 4 s. The incident energy was 17.3 keV, and the exit angle was 45°. We successfully observed the basic stripe domains and several lancet domains.

5. Surface X-ray diffraction

The third experimental hutch is equipped with a surface X-ray diffractometer connected with a molecular-beam-epitaxy (MBE) chamber [16-18]. This instrument is designed for *in situ* studies on III-V group semiconductor surfaces, especially surface crystallography under MBE conditions and growth dynamics of multilayer and nanostructures. The III-V group semiconductors are nitrides such as GaN and InN and arsenides such as GaAs and InAs, which can grow by exchanging two-types of MBE chambers.

The nitride-MBE chamber with an upgraded vacuum pumping system enhanced the flow rate of nitrogen gas and achieved a 75% increase in the growth rate. This facilitates *in situ* structural analysis of the nitrides under high growth rate conditions as well as reduces the crystal growth time. Our recent activity on nitrides focuses on the evolution of lattice strain and the indium composition at the InGaN/GaN heterointerfaces.

Using the arsenide-MBE chamber, we performed *in situ* X-ray diffraction to investigate the evolution of lattice deformations in several heterostructures such as InGaAs/(InAs)/GaAs(111)A, GaAsSb/GaAs(001), and GaAs/Si(111). In particular, the InGaAs/(InAs)/GaAs(111)A multilayer structures should reduce the threading dislocation density in InGaAs films, but the behavior of lattice deformation during crystal growth remains unclarified. As a result of *in situ* X-ray diffraction, we found that InGaAs directly grown on GaAs(111)A shows an anomalous lattice shrinkage along the *c*-axis without affecting the indium composition at the initial growth phase [19]. Conversely, the InGaAs grown on InAs/GaAs(111)A does not show initial lattice distortion, but a variable indium composition. Moreover, the evolution of the diffraction peak broadening was also monitored. The results confirm that the thin InAs layer effectively improves the crystal quality during the initial growth of InGaAs.

Takaya Mitsui[*1], Kenji Ishii[*1], Toshiya Inami[*1] and Takuo Sasaki[*2]

[*1] Magnetism Research Group, National Institutes for Quantum and Radiological Science and Technology

[*2] Coherent X-ray Research Group, National Institutes for Quantum and Radiological Science and Technology

References:

[1] P. Gütlich et al., Springer, Berlin (2011).

[2] Website of the Mössbauer Effect Data Center. http://www.medc.dicp.ac.cn/Resources.php (2019). Accessed 21August 2019.

[3] S. L. Ruby, *J. Phys. (Paris), Colloq.* **35**, C6-209-C6-211 (1974).

[4] R. L. Cohen et al., *Phys. Rev. Lett.* **41**, 381-384 (1978).

[5] O. C. Kistner et al., *Phys. Lett.* **5**, 299 (1963).

[6] E. Brownie et al., *Nuclear Data Sheets* **145**, 25-340 (2017).

[7] G. Kandl et al., *Z. Phys.* **226**, 103-115 (1969).

[8] D. Bessas et al., *Phys Rev. Lett.* **113**, 147601 (2014).

[9] P. Quarterman et al., *Nature comm.* **9**, 2058 (2018).

[10] K. Takubo et al., *Phys. Rev. B* **97**, 205142 (2018).

[11] K. Ishii et al., *J. Phys. Soc. Jpn.* **88**, 075001 (2019).

[12] H. Niwa et al., *Appl. Phys. Express* **12**, 052005 (2019).

[13] S. Kusano et al., *Nanomaterials* **9**, 642 (2019).

[14] Diego Casa, private communication.

[15] T. Inami, *Phys. Rev. Lett.* **119**, 137203 (2017).

[16] M. Takahasi et al., *J. Appl. Phys.* **41**, 6247 (2002).

[17] M. Takahasi, *J. Phys. Soc. Jpn.* **82**, 021011 (2013).

[18] T. Sasaki et al., *Jpn. J. Appl. Phys.* **55**, 05FB05 (2016).

[19] T. Sasaki et al. *J. Cryst. Growth* **512**, 33 (2019).